Inertial Measurement Unit Calibration Procedure for a Redundant Tetrahedral Gyro Configuration with Wavelet Denoising

Élcio Jeronimo de Oliveira[1,2,*], Waldemar de Castro Leite Filho[1], Ijar Milagre da Fonseca[2]
[1]Instituto de Aeronáutica e Espaço - São José dos Campos/SP – Brazil
[2]Instituto Nacional de Pesquisa Espacial - São José dos Campos/SP – Brazil

Abstract: *The aim of this paper was to present a calibration procedure applied to an inertial measurement unit composed of a triad of accelerometers and four gyros in a tetrad configuration. The procedure has taken into account a technique based on least-square methods and wavelet denoising to perform the best estimate of the sensor axis misalignments. The wavelet analysis takes place in order to remove undesirable high frequency components via multi-resolution signal decomposition analysis applied gyro signals. Equations for the least-square methods and wavelets analysis are presented, and the procedure is experimentally verified.*

Keywords: *Inertial measurements unit, Fiber optic gyro, Wavelet, IMU tetrad, IMU calibration.*

INTRODUCTION

The main error sources in the inertial navigation computation are associated with the sensor biases and scale factors, as well as the overall misalignments of the sensor configurations. Therefore, a method and an error model for inertial measurement unit (IMU) calibration are required. In order to design a proper method and an error model, spectral analysis and wavelet denoising were performed to highlight the long-term component and to remove high-frequency disturbances. Generally, the performance of the method is verified by comparison between a reference command and sensor computations, after error compensation (Cho and Park, 2005). In this work, it was used a parity vector analysis to verify the overall performance of the calibration. Such analysis was possible due to a redundant sensor that holds the existence of the parity vector. The performance analysis, based on parity vector, allows us to verify the amount of alignment error in any direction of rotation. In the sequence, this paper has developed the geometric, parity vector, and error model formulations, the wavelet application, the calibration technique, and the experimental results.

GEOMETRIC CONFIGURATION ANALYSIS

Geometry

The geometrical arrangement used in this work considers four gyros mounted on the faces (black hexagon) of a tetrahedral structure (tetrad), and three accelerometers in a triad configuration (blue block) internally fixed in the tetrahedral. The analysis performed here takes into account the gyros only, and the extension for accelerometers can be made easily. The tetrad configuration is shown in Fig. 1.
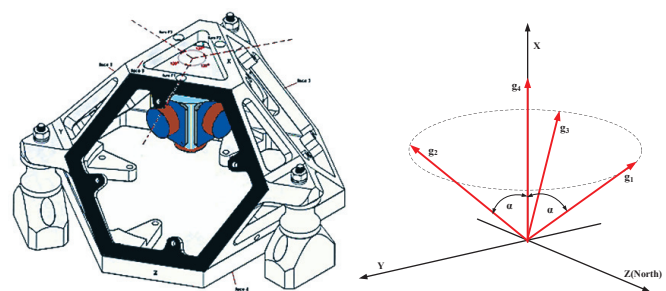

Figure 1. Tetrahedral base

The mathematical representation of the gyro arrangement is given in terms of measurement matrix, where each line represents the direct cosines vector of the sensor axis with respect to analytical triorthogonal axes (analytical triad). Therefore, considering the schematic represented in Fig. 1,

where $\alpha = 54.736°$, the measurement matrix is given by Eq. 1:

$$H = \begin{pmatrix} 1/\sqrt{3} & 0 & \sqrt{6}/3 \\ 1/\sqrt{3} & \sqrt{2}/2 & -\sqrt{6}/6 \\ 1/\sqrt{3} & -\sqrt{2}/2 & -\sqrt{6}/6 \\ 1 & 0 & 0 \end{pmatrix} \tag{1}$$

The matrix $\mathbf{H}$ relates the sensor measurements (g_i) with the angular rate in the main axes in the form of the eq. (2).

$$g_o = \mathbf{H}\omega \tag{2}$$

The estimate of the angular rate components in the main axes can be obtained from Eq. 2, as in Eqs. 3 and 4:

$$\hat{\omega} = \mathbf{H}^* \, g_o \tag{3}$$
$$\mathbf{H}^* = (\mathbf{H}^T \mathbf{H})^{-1} \mathbf{H}^T \tag{4}$$

where, the superscript (^{T}) indicates the transpose; $g_o = [g_1 \, g_2 \, g_3 \, g_4]^T$ is the vector of the gyro outputs; $\omega = [\omega_x \, \omega_y \, \omega_z]^T$ is the vector of angular rate about main axes; ω is the angular rate estimate vector; and $\mathbf{H}^*$ is the generalized inverse of $\mathbf{H}$.

Equation 4 provides the best state estimation in the least square sense.

Parity vector

The sensor equation considered in Eq. 2 can be rewritten with addition of faults, biases and noise components as in Eq. 5:

$$\tilde{g}_o = \mathbf{H}\omega + \delta g_o + \mathbf{f} + \eta_s \tag{5}$$

where, $\delta\mathbf{g}_o$ is a constant term (bias) vector; $\mathbf{f}$ is the fault vector; and η_s is a random term vector (Gaussian noise and other random disturbances).

Applying the singular value decomposition (SVD) on $\mathbf{H}$, the range and null spaces from this matrix can be obtained (Shim and Yang, 2004). In addition, it can also compute the biases influence on the arrangement. Decomposing $\mathbf{H}$ as Eqs. 6 and 7:

$$\mathbf{U}^T \mathbf{H} \mathbf{V} = \mathbf{\Lambda} = \begin{pmatrix} \Sigma \\ \mathbf{0} \end{pmatrix} \tag{6}$$

$$\mathbf{H} = \mathbf{U}\mathbf{\Lambda}\mathbf{V}^T \tag{7}$$

where, $\mathbf{U}$, $\mathbf{\Lambda}$, and $\mathbf{V}^T = \mathbf{V} = \mathbf{I}_n$ are matrices obtained from SVD of $\mathbf{H}$.

The matrix $\mathbf{\Sigma}$ is a diagonal one, whose elements are eigenvalues of $\mathbf{H}$.

Applying Eq. 7 into 5 and multiplying both sides by $\mathbf{U}^T$, it can be obtained the relationship as in Eq. 8:

$$\mathbf{U}^T \tilde{g}_o = \mathbf{\Lambda}\mathbf{V}^T \omega + \mathbf{U}_1^T (\delta g_o + \mathbf{f} + \eta_s) \tag{8}$$

Partitioning $\mathbf{U}$ as Eq. 9:

$$\mathbf{U} = [\mathbf{U}_1 \vdots \mathbf{U}_2] \tag{9}$$

where $\mathbf{U}_1 \in \mathbb{R}^{4\times3}$ and $\mathbf{U}_2 \in \mathbb{R}^{4\times1}$, and applying it into Eq. 8, the resulting equations can be written as Eqs. 10 and 11:

$$\mathbf{U}_1^T \tilde{g}_o = (\Sigma\mathbf{V})\omega + \mathbf{U}_1^T (\delta\mathbf{g}_o + \mathbf{f} + \eta_s) \tag{10}$$

$$\mathbf{U}_2^T \tilde{g}_o = \mathbf{U}_2^T(\delta\mathbf{g}_o + \mathbf{f} + \eta_s) \tag{11}$$

Equation 10 leads to a least square estimate of $\boldsymbol{\omega}$. In actual situations, bias, fault, and random-term vectors are unknown and defined as zero. This estimate is equivalent to Eq. 3, and can be expressed by Eq. 12:

$$\hat{\omega}_{LS} = (\Sigma\mathbf{V})^{-1}\mathbf{U}_1^T \tilde{g}_o \tag{12}$$

The meaning of Eq. 11 is that, if sensors faults and biases are zero, the resulting product of parity vector with sensor measurements is a white noise with zero mean. Otherwise, if the biases and/or faults values differ from zero, Eq. 11 is a "weighted" sensor errors summation. Then, $\mathbf{U}_2^T$ is the parity vector ($\mathbf{v}$) obtained from null space of $\mathbf{H}$.

MISALIGNMENT ERROR EQUATION

The estimation of the sensor axis misalignments takes an important role on the IMU construction. They are disagrees between predicted (or nominal) sensor axis angles and actual ones after built. Consequently, these alignment errors must be estimated and incorporated to perform a new sensor matrix. In addition, the scale factor is another important element to be estimated, and it can be performed in the same experiment.

In this work, a method based on least square technique was used (Cho and Park, 2005) to estimate misalignments and scale factors of the sensors, and the experimental procedures to obtain the proper sensor outputs for calibration were executed on 2-degree-of-freedom (DOF) turntable.

The IMU is composed of four gyros, as shown in Fig. 1, and, in order to design a proper error model, this arrangement

164

J. Aerosp. Technol. Manag., São José dos Campos, Vol.4, No 2, pp. 163-168, Apr.-Jun., 2012

is divided into two subsystems. The first one is composed of gyros g_1, g_2 and g_3 in a triorthogonal configuration, and the second one is composed of gyro g_4, whose measurement axis is collinear to the vertical X-axis. Therefore, the error modeling can be mathematically expressed as Eq. 13:

$$S_F g_v = MH\omega + b + \eta \qquad (13)$$

where, S_F is a diagonal matrix whose elements are the sensor scale factors in (⁰/s)/mV, g_v is the sensor outputs in mV, M is the misalignment matrix, and b is the bias vector;

The misalignment matrix (M) can be seen as a rotation from nominal sensor axes position to the real one. Separating Eq. 13 into two subsystems, there is Eq. 14:

$$\begin{bmatrix} S_{F1} g_{v1} \\ S_{F2} g_{v2} \\ S_{F3} g_{v3} \\ \hline S_{F4} g_{v4} \end{bmatrix} = \begin{bmatrix} M_1 & 0_{3\times3} \\ \hline 0_{1\times3} & M_2 \end{bmatrix} \begin{bmatrix} H_1 \\ \hline H_2 \end{bmatrix} \begin{bmatrix} \omega_x \\ \omega_y \\ \omega_z \end{bmatrix} + \begin{bmatrix} b_1 \\ b_2 \\ b_3 \\ \hline b_4 \end{bmatrix} + \eta \qquad (14)$$

where,

$$M_1 = \begin{bmatrix} m_{11} & m_{12} & m_{13} \\ m_{21} & m_{22} & m_{23} \\ m_{31} & m_{32} & m_{33} \end{bmatrix}; M_2 = [m_{4x}\, m_{4y}\, m_{4z}]; H_1 = \begin{bmatrix} h_{1x} & h_{1y} & h_{1z} \\ h_{2x} & h_{2y} & h_{2z} \\ h_{3x} & h_{3y} & h_{3z} \end{bmatrix}; H_2 = I_3$$

At this point, some remarks are needed to clarify Eq. 14:

- the misalignment of g_4 is estimated independently of the other sensors, and it is considered, without loss of generality, as a part of triorthogonal arrangement (pseudo-arrangement) coincident with the main axes;
- in spite of matrix H has 4×3 dimension, it is extended to accommodate the axes y and z in order to permit the estimate of misalignment between g_4 and those two axes;
- at a first glance, the matrix M could be 4×4 dimensional, given H has 4×3 dimension; however, this consideration would lead to singularity in the method.

Equation 15 is the Eq. 14 rewritten in a compact form:

$$S_{Fi} g_{vi} = [m_{ia}\, m_{ib}\, m_{ic}] H_j \omega + b_i + \eta_i \qquad (15)$$

where,
i = 1, 2, 3, 4 – is the sensor number;
j = 1,2 – is the sensor subsystem; for $\begin{cases} j = 1 \rightarrow a = 1, b = 2, c = 3 \\ j = 2 \rightarrow a = x, b = y, c = z \end{cases}$

Defining the difference between two successive sequences by $\omega_l^{(+)} - \omega_l^{(-)}$, where $l = x, y, z$ and $\omega^{(+/-)}$ is the positive/negative commanded turntable rate, the following vectors can

be constructed (Eq. 16):

$$\begin{bmatrix} r_a \\ r_b \\ r_c \end{bmatrix} = H_j \begin{bmatrix} \omega_x^{(+)} & -\omega_x^{(-)} \\ \omega_y^{(+)} & -\omega_y^{(-)} \\ \omega_z^{(+)} & -\omega_z^{(-)} \end{bmatrix} \qquad (16)$$

Using Eqs. 15 and 16, after some manipulations, it can be reached to a relationship expressed in Eq. 17.

$$[g_{vi}^{(+)} - g_{vi}^{(-)}] = [r_a r_b r_c] \begin{bmatrix} m_{ia}/S_{Fi} \\ m_{ib}/S_{Fi} \\ m_{ic}/S_{Fi} \end{bmatrix} + \eta_i \qquad (17)$$

Performing k evaluations (k≥3) for Eq. 17, it can be obtained Eq. 18,

$$\begin{bmatrix} m_{ia}/S_{Fi} \\ m_{ib}/S_{Fi} \\ m_{ic}/S_{Fi} \end{bmatrix} = (R^T R)^{-1} R^T \overline{G} \qquad (18)$$

where,

$$R = \begin{bmatrix} r_a(1) & r_b(1) & r_c(1) \\ \vdots & \vdots & \vdots \\ r_a(k) & r_b(k) & r_c(k) \end{bmatrix} \text{ and } \overline{G} = \begin{bmatrix} \bar{g}_{vi}(1) - \bar{g}_{vi}(2) \\ \bar{g}_{vi}(3) - \bar{g}_{vi}(4) \\ \vdots \\ \bar{g}_{vi}(n-1) - \bar{g}_{vi}(\eta) \end{bmatrix}$$

and g_{vi} is the mean value of the *ith* sensor measurement, k is the number of r-vectors, and n is the number of commanded sequences on two-axis table.

In order to solve Eq. 18, the constraint in Eq. 19 is necessary,

$$m_{ia}^2 + m_{ib}^2 + m_{ic}^2 = 1 \qquad (19)$$

After estimating the scale factors and misalignments, and rewritten Eq. 13, the sensor biases can be obtained as in Eq. 20:

$$\frac{1}{n} \sum_1^n (S_F(\bar{g}_v)_n - \tilde{H}\omega_n) = \bar{b} \qquad (20)$$

where, $\tilde{H}=MH$, $\overline{b}$ is the mean value of bias, and $(g_v)_n$ is the mean value of sensor output at *nth* turntable sequence.

The gyros used in the IMU (FOG) have biases with the same order of the Earth rotation rate (Ω_E). Thus, it is a complicated task to separate one from another in a skewed sensor configurations. In Eq. 20 this problem is solved by performing the average value of the residue, given by $(S(g_v)_n - H\omega_n)$, where the Ω_E influence is eliminated. This procedure will be clear

after displaying wavelet multi-resolution decomposition of the sensor outputs, and after being proved by parity vector analysis.

WAVELET TRANSFORM

After analyzing the spectral content and detecting the presence of long-term components in the sensor outputs, the wavelet analysis was chosen in order to eliminate undesirable high-frequency components and to highlight these long-terms (denoising).

Wavelet analysis has been used in a wide range of applications in signal processing techniques, due to its particular properties, such as compressing and denoising with low degradation of the original signal, time-scale representation, application in real-time operations in nonstationary signals, and by exposing hidden aspects of the signals like discontinuities, breakdown points, and trends (El-Sheimy and Nassar, 2004).

The theoretical foundations that hold the generalization and applicability of wavelet analysis to nonstationary signals can be found in Daubechies (1992), Mallat (1989) and Strang and Nguyen (1996).

The orthogonality properties of the discrete wavelet transformation make possible the multi-resolution decomposition of any time series (Daubechies, 1992). In the multi-resolution process, a complex function is decomposed at several levels of approximations or resolutions, where low- and high-pass filters in a filter bank configuration perform the discrete wavelet transformation at each level. In this scheme, the high-pass filters are responsible for details, while the low-pass ones are responsible for approximations. Some details contain noise components of high-frequency and others disturbances. In the approximations, there are long-term components, and thus include frequency components of the Earth rotation rate. At each level, the cutoff frequency (f_c) of the filter is one-half of the maximum frequency components into the previous level. Therefore, considering that the output of sensor is sampled (f_s) at 100 Hz, the maximum frequency component in the signal is 50 Hz ($f_s/2$), and at each level, the cutoff frequency is given by $(f_c)_i = f_s/2^{(i+1)}$, where i represents the level of decomposition.

The analyses performed here considered eight levels of decomposition, which indicates a filtering about 0.2 Hz. In this work, the choice of wavelet family was based on properties of continuity, detection of transient singularities, and slow moving anomalies. In this context, the Daubechies (db) wavelet family has been used in several works (Kim, Kim, Park, 2007), and, in the same way, it was also chosen for our purpose.

DATA ACQUISITION PROCEDURE

In order to obtain misalignment, scale factor and bias estimates from Eq. 17 to 20, a sequence of previously defined turntable commands is required to perform the matrix R formed by elements computed in Eq. 16. Once matrix R has rank three, it is not possible to estimate the IMU errors in one step only, forcing the IMU partition into two sub-IMU, and consequent considerations that hold the remarks and the model represented by Eq. 14. After denoising with wavelet algorithm, the gyro outputs are computed by error model equations, which obey the turntable sequence given in Table 1.

Table 1. Sequence of commanded rates (w=ω_{rt}; C=ω_{rt} cos (30º) and S=ω_{rt} sin (30º).

Sq.	Rot.axis		Input rate		
n	Inner	Outer	X	Y	Z
1	+w	0°	+w	0	0
2	-w	0°	-w	0	0
2	-w	0°	-w	0	0
3	+w	+180°	+w	0	0
4	-w	+180°	-w	0	0
5	0º	^+w	0	+w	0
6	0º	-w	0	-w	0
7	-30º	+w	0	+w	0
8	+180º	-w	0	-w	0
9	+90º	+w	0	0	+w
10	+90º	-w	0	0	-w
11	-90º	^+w	0	0	+w
12	-90º	-w	0	0	-w
13	+30º	+w	0	+C	+S
14	+30º	-w	0	-C	-S
15	-30º	+w	0	+C	-S
16	-30º	-w	0	-C	+S

Notice that calibration procedures of tetrahedral base with FOG was performed on the two-DOF rotate table (BD267) with attitude error less than 1×10^{-3} degree, and rate error less than 1×10^{-3} degree/second. The rate (ω_{rt}) used for calibration procedure was 10%. The method could be executed with only six sequences (two rotation directions per axis); however, 16 sequences were employed aiming at minimizing turntable error effects and error covariance matrix ($[\mathbf{R}^T\mathbf{R}]^{-1}$). The block diagram of the acquisition system is shown in Fig. 2. The ensemble is composed by

four FOG connected to an embedded computer PC104 via bus RS232 asynchronous, which performs the acquisition and data storage. After the execution of commanded sequences is finished (Table 1), data are transferred to a personal computer via FTP communication and processed according to the error model.
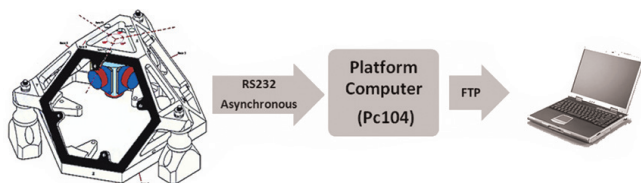

Figure 2. Block diagram of the calibration set (data acquisition).

RESULTS

After denoising the output signals, the long-term components are highlighted and represent the earth rotation rate (Fig. 3), which modulates the gyro outputs of the sequences, from $k=3$ to $k=8$ ($n=5{:}16$, $k=3$ results from $(gv)_{n=5}$ - $(gv)_{n=6}$ and $k=8$ results from $(gv)_{n=15}$ - $(gv)_{n=16}$) related to outer axis rotation. With this group of measurements, the mean value estimated for Ω_E was 15.8721°/h, which represents a good approximation with the actual one. The modulation level at each output is related to the sensor position, and the frequency is related to the turntable rate.
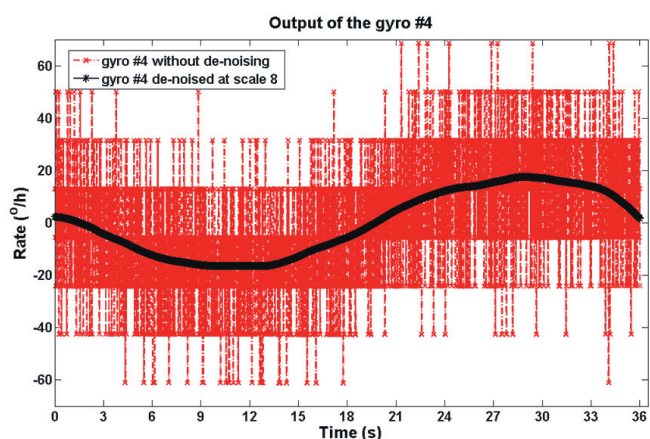

Figure 3. Output of the gyro #4. Original (red); de-noised with db4 at scale 8 (black).

Considering that the integration of modulation signal for integer numbers of cycles about the outer axis is zero, the mean value of the gyro outputs in this condition will contain, basically, the commanded rate and biases.

Therefore, Eq. 20 applied in the sequences from $n=5$ to $n=16$ holds the estimation of the mean values of the biases.

Figure 4 illustrates the stability of the bias determination from $k=3$. The plot was obtained from the product of the corrected parity vector (Eq. 25) with the mean value of the gyro outputs combined to remove ω_{rt} (g_b), as in Eq. 21.

$$\mathbf{v}_c \bar{\mathbf{g}}_b = \mathbf{v}_c \left[\frac{1}{2} \mathbf{S}_F ((\bar{\mathbf{g}}_v)_n + (\bar{\mathbf{g}}_v)_{n+1}) \right] \qquad (21)$$

$$\mathbf{v}_c \bar{\mathbf{g}}_\omega = \mathbf{v}_c \left[\frac{1}{2} \mathbf{S}_F ((\bar{\mathbf{g}}_v)_n + (\bar{\mathbf{g}}_v)_{n+1}) \right] \qquad (22)$$

$$\mathbf{v} \bar{\mathbf{g}}_\omega = \mathbf{v} \left[\frac{1}{2} \mathbf{S}_F ((\bar{\mathbf{g}}_v)_n + (\bar{\mathbf{g}}_v)_{n+1}) \right] \qquad (23)$$

$$\mathbf{v} = \mathbf{U}_2^T = [\,-0.408250 \quad -0.40825 \quad -0.408250 \quad 0.70711] \quad (24)$$

$$\mathbf{v}_c = [\,-0.40955 \quad -0.40903 \quad -0.40585 \quad 0.70729] \qquad (25)$$

$$\mathbf{M}_1 = \begin{bmatrix} 0.9999895 & -0.0019974 & 0.0041171 \\ 0.0004597 & 0.9999998 & -0.0004378 \\ -0.0009892 & 0.0003843 & 0.9999994 \end{bmatrix} \qquad (26)$$

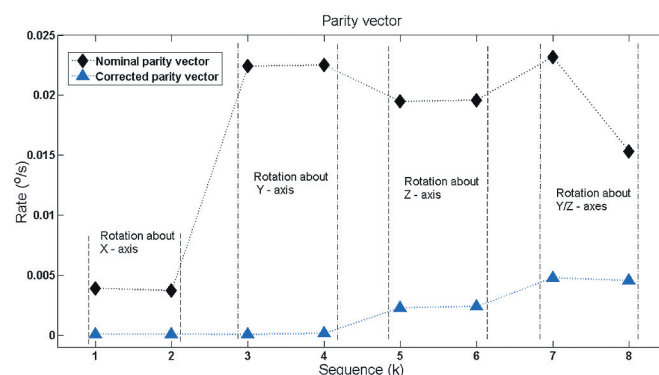$$\mathbf{M}_2 = [0.99999 \quad 0.0010024 \quad 0.0016921]$$

Figure 4. Absolute mean value of parity vector of sequences $k(\omega^{(+)} - \omega^{(-)})$ without bias and Ω_E.

In addition, for comparison, it was plotted the product of the estimated biases (Eq. 20) with corrected parity vector ($v_c b$). The results obtained for bias and scale factor are shown in Table 2, and they are compared with results obtained for the same FOG in the individual calibration (Silva, 2010). Therefore, the individual calibration was made in a different set, location and time. The results obtained for tetrad are quite consistent. For the FOG used in this work, the nominal value of the scale factor was 24mV/°/s. The misalignment matrices (M_1 and M_2) are given in Eq. 26.

Table 2. Results from individual sensor and tetrad calibrations.

Gyro	Individual calibration (+20º/s)		Tetrad calibration (+10º/s)	
#	Bias (º/s)	S_F (mV/º/s)	Bias (º/s)	S_F (mV/º/s)
1	0.0020795	26.5912	0.0015563	26.6259
2	0.0027427	25.9534	0.0024357	26.0274
3	0.0034507	26.0316	0.0031409	26.0730
4	0.0020057	26.6659	0.0015402	26.7118

In order to evaluate the improvement of the calibration procedure, and considering that the parity equation should result in a white noise with zero mean, it was plotted in the Fig.5 the results of Eqs. 22 and 23, which take into account the commanded rate only (bias and ω_E are removed). In that condition, the difference between nominal and corrected parity equations reveal the misalignments influence only. Bear in mind that, in some situations, not all sensors are excited when the rate is applied on one of the main axes and, in the same way, if the misalignments plane is orthogonal to the input axis (commanded rate), it will not appear. Therefore, this approach allows us to evaluate the improvement of the misalignment estimates in all directions in one step. It is clear, in Fig.5, the improvement of the method; however, a small residual error in the sequences $k=5$ to $k=8$ remains.
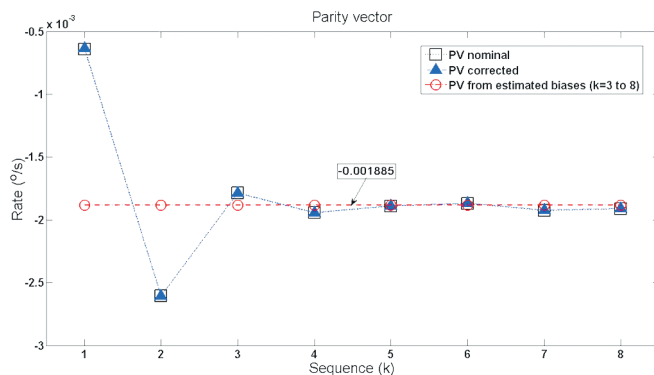

Figure 5. Mean value of parity vector of sequences k($\omega^{(+)}$-$\omega^{(-)}$) without ω_{rt}

CONCLUSIONS

In this paper, a method based on least square parameter estimation was used to estimate the misalignments of an IMU in a tetrad configuration, and parity equations were also used to evaluate the quality of the calibration. In this arrangement, the parity equations do not provide the individual misalignment residue, but they indicate the amount of error in the overall estimation process in any direction that the system may be excited. Therefore, it is a good index of quality in the calibration process. In addition, the parity equation analysis will give support to fault detect algorithms in terms of threshold determination, consequently, reducing the false alarm probability. When compared with individual calibration, the results obtained by this method are quite consistent, and denote the quality of the methodology used.

REFERENCES

Cho, S. Y., Park, C. G., 2005, "A calibration technique for a redundant imucontaining low-grade inertial sensors", ETRI Journal, Vol. 27, No. 4, pp. 418-425.

Daubechies, I., 1992, "Ten lectures on wavelets", Philadelphia, SIAM.

El-Sheimy, N., Nassar, S., 2004, "Wavelet de-noising for IMU alignment", IEEE A&E Systems Magazine, pp. 32-39.

Kim, S., Kim, Y., Park, C., 2007, "Failure diagnosis of skew-configured aircraft inertial sensors using wavelet decomposition", IET Control Theory and Applications, Vol. 1, pp. 1390-1397.

Mallat, S. G., 1989, "A theory of multiresolution signal decomposition: the wavelet representation", IEEE Transactions on Pattern Analysis and Machine Intelligence, Vol. 11, pp. 674-693.

Shim, D. S., Yang, C. K., 2004, "Geometric FDI based on SVD for redundant inertial sensor systems", 5th Asian Control Conference, Vol. 2, pp. 1094-1100.

Silva, J. F.F., 2010, "Procedimentos para ensaios de caracterização de giro de fibra óptica", Technical Report ASE-MT-001-2010, Instituto de Aeronáutica e Espaço, IAE, Brasil.

Strang, G., Nguyen, T., 1996, "Wavelets and filter banks", Wellesley, MA, Cambridge Press.